

Bi₂CoO₂F₄—A Polar, Ferrimagnetic Aurivillius Oxide-Fluoride

Euan A. S. Scott, Eleni Mitoudi Vagourdi, Mats Johnsson, Vanessa Cascos, Filbin John, Dave Pickup, Alan V. Chadwick, Hania Djani, Eric Bousquet, Weiguo Zhang, P. Shiv Halasyamani, and Emma E. McCabe*



Cite This: *Chem. Mater.* 2022, 34, 9775–9785



Read Online

ACCESS |



Metrics & More

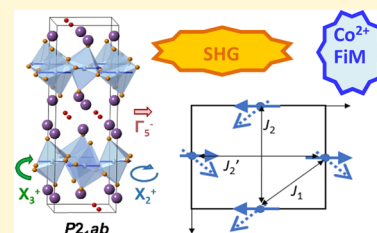


Article Recommendations



Supporting Information

ABSTRACT: Aurivillius oxides have been a research focus due to their ferroelectric properties, but by replacing oxide ions by fluoride, divalent magnetic cations can be introduced, giving Bi₂MO₂F₄ (*M* = Fe, Co, and Ni). Our combined experimental and computational study on Bi₂CoO₂F₄ indicates a low-temperature polar structure of *P2₁ab* symmetry (analogous to ferroelectric Bi₂WO₆) and a ferrimagnetic ground state. These results highlight the potential of Aurivillius oxide-fluorides for multiferroic properties. Our research has also revealed some challenges associated with the reduced tendency for polar displacements in the more ionic fluoride-based systems.



INTRODUCTION

Designing and preparing new multiferroic and magnetoelectric phases (with both polar and magnetic order) is an ongoing challenge in materials chemistry and physics.^{1,2} The Aurivillius oxides are well-known ferroelectrics,^{3,4} but it has proved challenging to introduce high concentrations of magnetic ions into these phases.^{5–9} Aurivillius materials, of general formula Bi₂A_{*n*–1}B_{*n*}O_{3*n*+3} (with *A* typically group 2 or lanthanide or Bi, Pb cations; *B* typically d⁰ transition metal ions in high oxidation states), adopt layered perovskite-related structures composed of fluorite-like [Bi₂O₂]²⁺ layers separating perovskite-like blocks *n* layers thick (Figure 1). The ideal aristotype structure is tetragonal, but Aurivillius phases often adopt lower-symmetry distorted structures, which allow in-plane polarizations and rotations of BO₆ octahedra.^{7,10,11} These distortions occur in part to optimize cation coordination environments and to relieve strain in stacking the slightly wider perovskite-like blocks with the more narrow [Bi₂O₂]²⁺ layers.¹²

These distortions can be discussed in the context of the *n* = 1 Aurivillius oxide Bi₂WO₆. Its aristotype high-symmetry structure would be of *I4/mmm* symmetry (*a_t* ≈ 3.8 Å, *c_t* ≈ 16.4 Å, where the subscript *t* denotes this ideal *I4/mmm* structure), although this ideal structure is never observed in practice—Bi₂WO₆ undergoes a reconstructive phase transition on warming above 950 °C.^{13,14} At intermediate temperatures, Bi₂WO₆ adopts a polar structure of *B2cb* symmetry, which allows rotations of WO₆ octahedra about an in-plane axis (about [110]_{*t*}), as well as polar displacements along this same axis (Figure 1).¹³ These distortions of odd-layer Aurivillius and Ruddlesden–Popper phases have been tabulated^{15,16} and can also be explored using web-based ISODISTORT software,¹⁷ and key distortions are illustrated in Figure 1 (see also the Supporting Information). The distortions can be described using irrep notation (where the letter denotes the *k*-point of the distortion, and the superscript indicates whether or not

inversion symmetry is preserved), and the rotations of BO₆ octahedra can also be described using Glazer notation.¹⁸ The intermediate *B2cb* structure of Bi₂WO₆ allows both X₃⁺ (*a⁻a⁻c⁰*) rotations of WO₆ octahedra and Γ₅⁻ in-plane polar displacements.¹³ On cooling below 670 °C, a second WO₆ rotation (X₂⁺, *a⁰a⁰c*) occurs, lowering the symmetry further to *P2₁ab*.^{13,19}

The more limited compositional flexibility of the Aurivillius phases (including the difficulties associated with introducing magnetic ions) compared with perovskite and Ruddlesden–Popper systems may relate to steric factors related to stacking strain¹² but could also arise from the polar displacements of the d⁰ *B*-site cations in Aurivillius materials,²⁰ which would be less favorable for magnetic dⁿ transition metal ions. Replacing some of the oxide ions by fluoride ions in *n* = 1 Aurivillius materials lowers the *B*-cation oxidation state required for charge balance^{21–23} and may also change the relative significance of polar displacements and rotations of octahedra.²⁴ This has allowed magnetic *n* = 1 Aurivillius oxide-fluorides Bi₂BO₂F₄ (*B* = Fe, Co, and Ni) to be prepared.^{25–27} The report of long-range magnetic order in Bi₂CoO₂F₄ (with the possibility of a ferromagnetic component)²⁵ motivated us to investigate it further. Mitoudi Vagourdi et al.²⁵ were able to use X-ray diffraction to confirm its *n* = 1 Aurivillius structure, but X-rays are relatively insensitive to the positions of the light O/F anions, making it difficult to investigate possible structural distortions further. We report here the structural character-

Received: September 7, 2022

Revised: October 3, 2022

Published: October 17, 2022



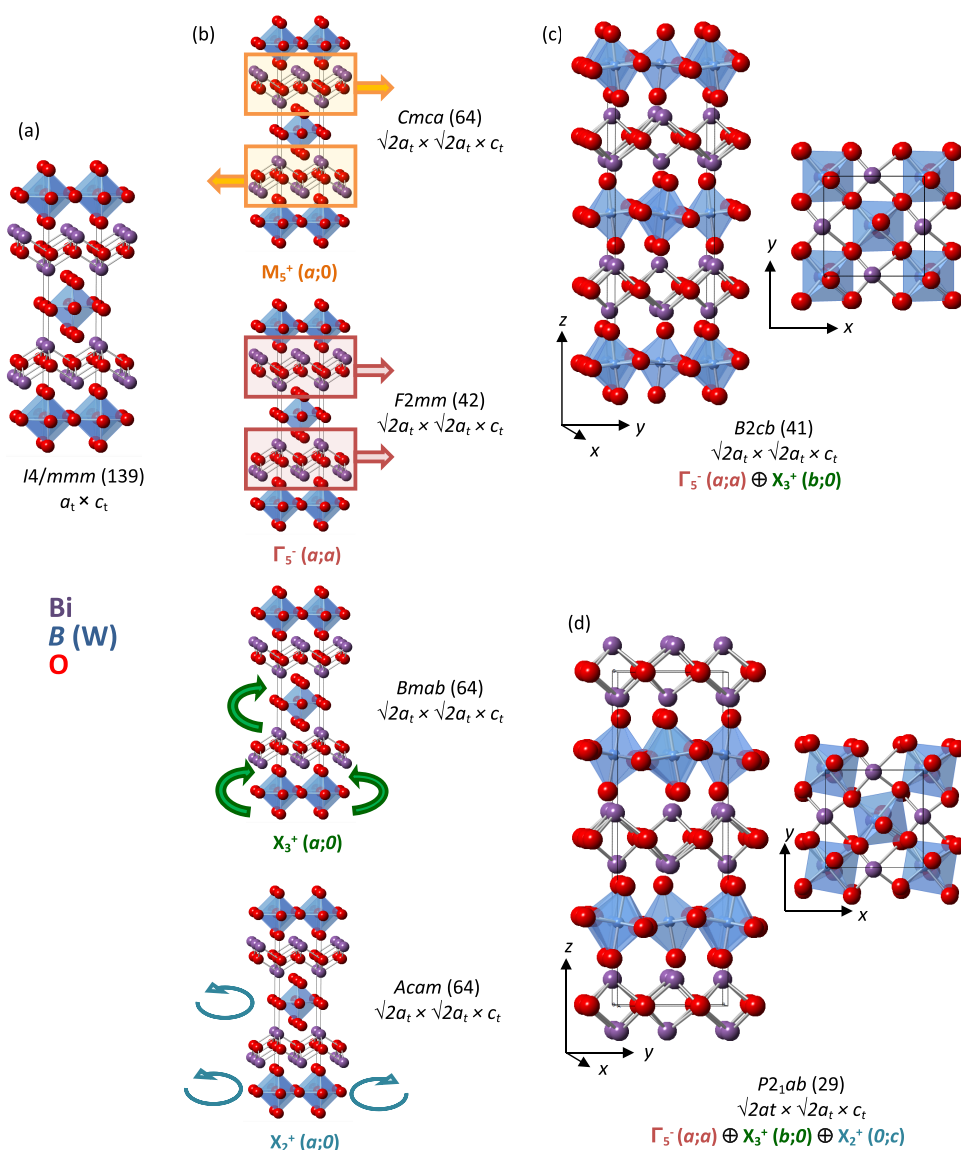


Figure 1. Illustration of (a) an ideal $I4/mmm$ structure for an $n = 1$ Aurivillius oxide and (b) schematic showing key structural distortions (order parameter directions for the irreps are given in parentheses) for this structure (and resulting space group symmetries); panel (c) shows the intermediate $B2cb$ structure of Bi_2WO_6 and panel (d) shows the low-temperature $P2_1ab$ model of Bi_2WO_6 . Bi, B/W, and O ions are shown in purple, blue, and red, respectively.

ization of $\text{Bi}_2\text{CoO}_2\text{F}_4$ using neutron powder diffraction (NPD) and second-harmonic generation (SHG) experiments, complemented by density functional theory (DFT) calculations. These methods reveal a distorted structure analogous to those adopted by ferroelectric Bi_2WO_6 . Low-temperature NPD data allow us to determine the long-range magnetic structure of $\text{Bi}_2\text{CoO}_2\text{F}_4$ and explain the field dependence reported by Mitoudi Vagourdi et al.²⁵

METHODS

Pink polycrystalline samples of $\text{Bi}_2\text{CoO}_2\text{F}_4$ were prepared hydrothermally, as described in ref 25. Variable temperature X-ray powder diffraction (XRPD) data were collected using a PANalytical Empyrean diffractometer with Cu $K_{\alpha 1}$ radiation (with a Ge monochromator), an X'Celerator detector, and an Oxford Cryosystems PheniX cryostat. 20 min scans were collected at 20 K intervals on warming from 12 to 300 K, with dwell times of 10 min for temperature equilibration before each scan.

NPD data were collected at the ISIS Neutron and Muon Source. One batch (0.84 g) was used to collect medium-resolution NPD data on the GEM diffractometer; the sample was placed in a cylindrical vanadium sample can (diameter of 6 mm) to a height of ~ 1 mm, and data were collected at 50 K and at 5 K. High-resolution NPD data were also collected on a second batch of sample (0.35 g) on the HRPD diffractometer; the sample was placed in a thin-walled vanadium can to a height of 1.9 cm, and data were collected at 5 K. Powder diffraction data were analyzed using Topas Academic software^{28,29} and ISODISTORT³⁰ was used to explore possible structural distortions and magnetic ordering arrangements. Jana2006 software³¹ was used for incommensurate refinements.

X-ray absorption near-edge structure data was obtained on the $\text{Bi}_2\text{CoO}_2\text{F}_4$ material using the B18-CORE XAS instrument at Diamond Light Source at the Harwell Science and Innovation Campus in Oxfordshire. XANES measurements of the Co K-edge were performed, and data was analyzed qualitatively to look at the oxidation state of the Co metal. Calibration of the energy scale was ensured by simultaneously collecting XANES data from a Co foil using a third ionization chamber.

$\text{Bi}_2\text{CoO}_2\text{F}_4$ was tested for an SHG signal using the experimental setup described in ref 32; $\text{Bi}_2\text{CoO}_2\text{F}_4$ powder was placed in a fused silica tube (with an outer diameter of 4 mm). Relevant comparisons with a known SHG material, $\alpha\text{-SiO}_2$, were made under the same conditions. A 1064 nm pulsed Nd:YAG laser (Quantel Laser, Ultra 50) generated the fundamental light, and the SHG intensity was recorded at room temperature using an oscilloscope (Tektronix, TDS3032).

Calculations were performed within DFT³³ using the ABINIT package.^{34,35} The projected augmented waves (PAW) approach³⁶ was used to represent the valence and core electrons. The exchange correlation energy functional was evaluated within both the local density approximation (LDA) and the generalized gradient approximation (GGA).³⁷ The atomic data set was taken from the JTH table³⁸ where 15 valence electrons were used for Bi ($5d^{10} 6s^2 6p^3$), 17 for Co ($3s^2 3p^6 3d^7 4s^2$), 6 for O ($2s^2 2p^4$), and 7 for F ($2s^2 2p^5$). The wave functions were expanded up to a maximum kinetic energy cutoff of 22 hartrees. Integrals over the Brillouin zone were approximated by sums on a $6 \times 6 \times 2$ Monkhorst–Pack mesh of special k -points. Spin-polarized structural optimizations were performed in LDA and GGA until the absolute values of the forces on atoms were converged to less than 10^{-5} Ha/bohr. The 3d electrons were corrected through the DFT + U approximation^{39,40} where different values of on-site Coulomb interaction U and site exchange interaction J were used to check the energy differences between spin configurations. Phonons were calculated using density functional perturbation theory within GGA-JTH.^{41,42}

RESULTS

XANES. XANES is a useful tool for determining oxidation states of transition metals by comparison of the absorption edge position with that from standards containing the transition metal in known oxidation states. The energy of the absorption edge increases with the oxidation of state of the transition metal since more energy is required to remove electrons from ions with higher charge. In this case, CoO, Co_3O_4 , Ba_2CoO_4 , and BaCoO_3 were chosen as standards with Co oxidation states of +2, +2.67, +4, and +4, respectively. Figure 2 shows the absorption edges of these reference materials and the $\text{Bi}_2\text{CoO}_2\text{F}_4$ sample. As expected, the energy of the absorption edges of the standards increases with oxidation state. The energy of the absorption edge of the $\text{Bi}_2\text{CoO}_2\text{F}_4$ sample, measured half way up the edge, is the same as that from CoO, indicating that the Co oxidation state in $\text{Bi}_2\text{CoO}_2\text{F}_4$ is close to +2. We note that the Co site in $\text{Bi}_2\text{CoO}_2\text{F}_4$ is thought to be coordinated by the more electronegative F^- anions rather than O^{2-} ions (see below and Mitoudi Vagourdi et al.²⁵), which may shift the Co K-edge position to slightly higher energies.⁴³ The observed edge position could therefore indicate a slightly lower cobalt oxidation state in our sample, but further work involving comparison with stoichiometric cobalt fluoride references is needed to confirm this.

Second Harmonic Generation. SHG measurements using 1064 nm radiation gave a signal for $\text{Bi}_2\text{CoO}_2\text{F}_4$ (about 0.4 times that of $\alpha\text{-SiO}_2$) (Figure 2); no laser damage was observed for the sample. This measurement indicates that $\text{Bi}_2\text{CoO}_2\text{F}_4$ must adopt an acentric structure at room temperature.

Preliminary Characterization Using XRPD Data. XRPD data were collected between 20 and 300 K to monitor unit cell parameters as a function of temperature. The data were fitted reasonably well by orthorhombic models considered for analysis of NPD data (see below), and the unit cell volume increased smoothly on warming (see the Supporting

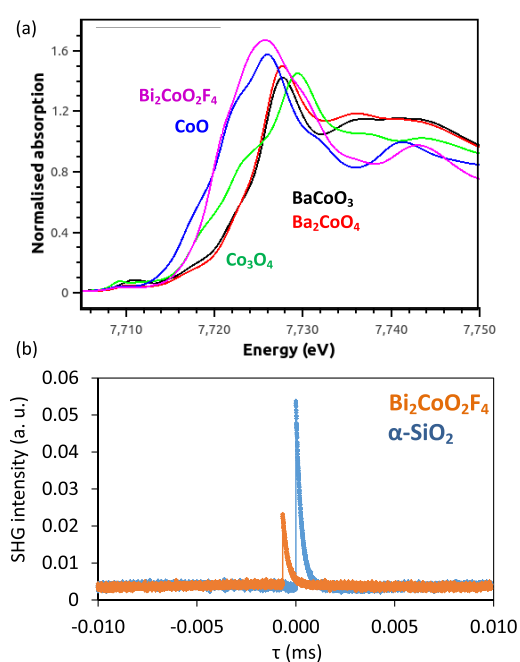


Figure 2. Panel (a) shows the X-ray absorption near-edge spectra (XANES) of $\text{Bi}_2\text{CoO}_2\text{F}_4$ (pink), CoO (blue), Co_3O_4 (green), BaCoO_3 and Ba_2CoO_4 (black and red) showing a cobalt oxidation state close to +2 in $\text{Bi}_2\text{CoO}_2\text{F}_4$; panel (b) shows the SHG signal for $\text{Bi}_2\text{CoO}_2\text{F}_4$ (orange) and compared with $\alpha\text{-SiO}_2$ (blue).

Information). There is a change in slope in the unit cell c parameter below 190 K (see the SI). This may indicate a structural change (e.g., a tilt transition) below this temperature as suggested from phonon analysis from Raman data,²⁵ but further structural analysis as a function of temperature is needed to confirm this.

Crystal Structure Determination from NPD Data. The main reflections observed in 50 K NPD data are consistent with an $n = 1$ Aurivillius phase, but additional reflections were also observed that cannot be indexed by the high-symmetry $I4/mmm$ ($a_i \approx 3.8$ Å, $c_i \approx 16.3$ Å) cell. These additional reflections are consistent with a larger $\sqrt{2}a_i \times \sqrt{2}a_i \times c_i$ unit cell. These superstructure reflections also rule out the non-centrosymmetric disordered model of $I4$ symmetry ($a \approx 3.8$ Å; $c \approx 16.3$ Å) reported by Mitoudi Vagourdi et al. from X-ray diffraction work.²⁵ The observation of superstructure reflections from neutron scattering data (with relatively stronger sensitivity to the positions of the light anions)⁴⁴ and not from careful X-ray studies (in which the scattering is dominated by the electron-rich Bi^{3+} sites) suggested that structural distortions involving displacements of the anion sites (such as rotations of the CoX_6 octahedra) should be considered. (Given the similar neutron scattering lengths of oxygen and fluorine (5.803(4) and 5.65(1) fm, respectively),⁴⁴ no attempt was made at this stage to determine the anion distribution over the three sites, and all were modeled as fully occupied by oxide ions.) ISODISTORT was used to explore possible distortions that might give rise to such a supercell. Mode inclusion analysis^{45–47} (see the Supporting Information) suggested that the lower-symmetry structure results from rotation of CoX_6 octahedra about an in-plane axis (described by $\text{irrep } X_3^+$; see Figure 1 and the Supporting Information), giving a model of $Bmab$ symmetry ($\bar{a}cb$ setting of space group 54, $Cmca$).

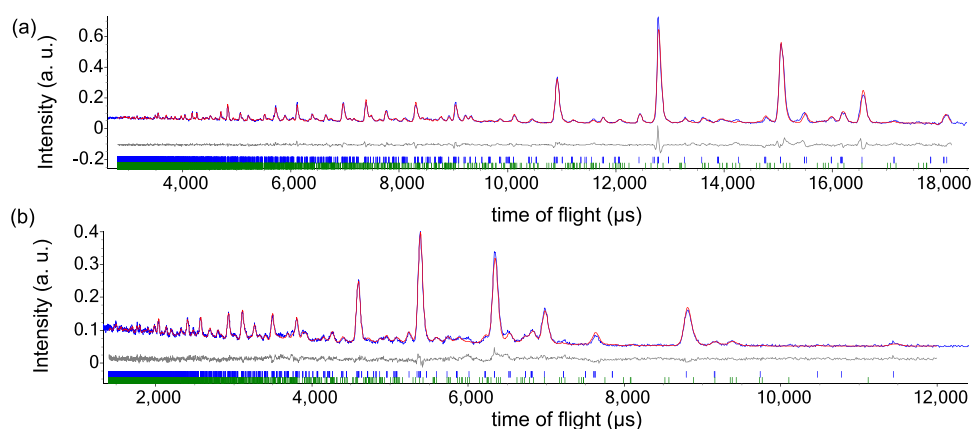


Figure 3. Details from Rietveld refinement using 50 K NPD data collected for $\text{Bi}_2\text{CoO}_2\text{F}_4$ using the $P2_1ab$ model with anion vacancies. The refinement was carried out using NPD data from the 91° (panel a) and 35° (panel b) banks with upper ticks (blue) and lower ticks (green) showing peak positions for $\text{Bi}_2\text{CoO}_2\text{F}_4$ (86(1)% by mass) and for $\text{Bi}_7\text{F}_{11}\text{O}_5$ (14(1)% by mass), respectively; $R_{\text{wp}} = 6.32\%$, $R_{\text{p}} = 4.64\%$, and $\chi^2 = 2.90\%$.

Table 1. Details from Rietveld Refinement Using 50 K NPD Data Collected for $\text{Bi}_2\text{CoO}_2\text{F}_4$ Using the $P2_1ab$ Model with Anion Vacancies^b

atom	site	x	y	z	occupancy	$U_{\text{iso}} \times 100$ (\AA^3)
Bi(1)	4a	0.004(6)	0.011(2)	0.0776(7)	1	1.7(2)
Bi(2)	4a	0.505(6)	0.009(2)	0.5771(7)	1	1.4(1)
Co	4a	0 ^a	0.976(4)	0.747(1)	1	0.6(2)
O/F(1) (eq)	4a	0.208(7)	0.290(3)	0.7865(7)	0.75	1.5(2)
O/F(2) (eq)	4a	0.806(7)	0.199(4)	0.2700(9)	0.76	2.7(4)
O/F(3) (ap)	4a	0.027(7)	0.929(4)	0.874(1)	1	2.3(3)
O/F(4) (ap)	4a	0.517(7)	0.933(4)	0.373(1)	0.81	2.0(4)
O/F(5) (fl)	4a	0.255(7)	0.243(3)	0.994(6)	1	1.7(3)
O/F(6) (fl)	4a	0.749(7)	0.256(3)	0.4996(6)	1	1.4(2)

^aCoordinate fixed to define the origin of the polar axis. ^bThe refinement was carried out using NPD data from the 91° and 35° banks and included $\text{Bi}_7\text{F}_{11}\text{O}_5$ impurity (14(1)% by mass). The $\text{Bi}_2\text{CoO}_2\text{F}_4$ main phase (86(1)% by mass) had unit cell parameters $a = 5.4343(5)$ \AA , $b = 5.4339(6)$ \AA , $c = 16.350(1)$ \AA and volume = $482.81(8)$ \AA^3 ; $R_{\text{wp}} = 6.32\%$, $R_{\text{p}} = 4.64\%$, and $\chi^2 = 2.90\%$. (Abbreviations “ap”, “eq”, and “fl” refer to “apical”, “equatorial”, and “fluorite”, respectively.)

Table 2. Details from Rietveld Refinement Using 5 K NPD Data Collected for $\text{Bi}_2\text{CoO}_2\text{F}_4$ Using the $P2_1ab$ Model (with Anion Vacancies) and $m\Gamma_2$ Magnetic Model^b

atom	site	x	y	z	occupancy	$U_{\text{iso}} \times 100$ (\AA^3)
Bi(1)	4a	0.006(4)	0.010(2)	0.0780(5)	1	0.1(1)
Bi(2)	4a	0.508(5)	0.009(2)	0.5767(6)	1	0.5(1)
Co	4a	0 ^a	0.980(4)	0.748(1)	1	0.2(2)
F(1)	4a	0.207(5)	0.290(3)	0.7847(7)	0.75	0.0(1)
F(2)	4a	0.805(6)	0.198(4)	0.2712(9)	0.76	1.9(4)
F(3)	4a	0.024(5)	0.928(3)	0.873(1)	1	1.3(3)
F(4)	4a	0.519(6)	0.933(4)	0.374(1)	0.81	0.9(4)
O(5)	4a	0.252(5)	0.241(2)	0.9941(6)	1	0.5(2)
O(6)	4a	0.743(5)	0.254(2)	0.4991(6)	1	0.1(1)

^aCoordinate fixed to define the origin of the polar axis. ^bThe refinement was carried out using NPD data from the 91° and 35° banks and included $\text{Bi}_7\text{F}_{11}\text{O}_5$ impurity (14% by mass). The $\text{Bi}_2\text{CoO}_2\text{F}_4$ main phase (86% by mass) has unit cell parameters $a = 5.4317(5)$ \AA , $b = 5.4313(5)$ \AA , $c = 16.348(1)$ \AA and volume = $482.30(7)$ \AA^3 with Co^{2+} moments of $2.5(1)$ μ_{B} ($2.37(1)$ μ_{B} along b and $0.7(2)$ μ_{B} along a); $R_{\text{wp}} = 5.83\%$, $R_{\text{p}} = 3.94\%$, and $\chi^2 = 14.2\%$.

The SHG activity observed (Figure 2) indicates that $\text{Bi}_2\text{CoO}_2\text{F}_4$ must adopt a non-centrosymmetric crystal structure, and so non-centrosymmetric, polar models (including those of $B2cb$ and $P2_1ab$ symmetry, analogous to Bi_2WO_6)¹³ were considered. This was consistent with mode inclusion analysis, which suggested a further improvement in fit if in-plane polar displacements (described by the Γ_5^- irrep), or rotation of CoX_6 octahedra about the long axis ($[001]_t$),

described by the X_2^+ irrep, were allowed (see the Supporting Information).

The model of $B2cb$ symmetry (cab setting of space group 41, $Aba2$) allows displacements along the polar a axis ($[110]_t$, where the subscript t denotes the high-symmetry $I4/mmm$ unit cell), as well as rotation of CoX_6 octahedra about this axis (described by the X_3^+ irrep). Lowering the symmetry further to $P2_1ab$ (cab setting of space group 29, $Pca2_1$) allows an

additional rotation of CoX_6 octahedra about the long axis ($[001]_i$) described by the X_2^+ irrep.

Both $B2cb$ and $P2_1ab$ models give good fits to the data at 50 K (R_{wp} of 6.64% (61 parameters) and 6.28% (79 parameters) for $B2cb$ and $P2_1ab$ models, respectively) (see the Supporting Information) but surprisingly high atomic displacement parameters for the equatorial anion site(s). In Rietveld refinements, atomic displacement parameters are often correlated with site occupancies, and so this could indicate vacancies on this site or a problem with the model in terms of the position of the site. For both models, refinements were carried out using a single global atomic displacement parameter and allowing occupancies of anion and cobalt sites to refine, while the bismuth site occupancies were fixed at unity. These refinements suggested significant vacancies on equatorial anion sites (other site occupancies refined to unity with two esds and so were fixed as fully occupied), similar to reports for $\text{LaSrCoO}_{3.5-x}$ ⁴⁸ (Site occupancies refined to values of 0.75(4), 0.76(4), and 0.81(1) for X(1), X(2), and X(4) sites, respectively.) Site occupancies were fixed at these values for subsequent refinements, and refining atomic displacement parameters for each site gave more physically reasonable values, and so it is likely that there are some anion vacancies in this sample of $\text{Bi}_2\text{CoO}_2\text{F}_4$. Allowing the atomic displacement parameter to refine anisotropically for this site in the $B2cb$ model did suggest some increased displacement (either static or dynamic) in the ab plane, which may indicate some further rotation of CoX_6 octahedra (e.g., about the long axis). Refinement details for $P2_1ab$ refinements using 50 K data are shown in Figure 3 and Table 1 and below (Table 2 and Figures 5 and 6) for refinements using 5 K data.

Bond valence sum calculations were used as a simplistic way to determine the likely anion distribution using 50 K bond lengths. (Bond valence sum parameters calculated for this low-temperature model should not be interpreted quantitatively as the parameters are determined from room temperature structures,^{49,50} but can be instructive for comparing between different ordering models.) Calculating apparent valences for equatorial and apical sites gave valences close to 1 (assuming either F or O occupancy), while higher valences closer to 2 were calculated for anion sites in the fluorite-like layers (full details are given in the Supporting Information). These values suggest that anion sites in the perovskite layers might be favored by F^- anions giving CoF_6 octahedra, while O^{2-} ions occupy sites in the fluorite-like $[\text{Bi}_2\text{O}_2]^{2+}$ layers. Taking into account the anion vacancies noted above, this suggests an approximate composition of $\text{Bi}_2\text{CoO}_2\text{F}_{3.32}$ compared with the target stoichiometry of $\text{Bi}_2\text{CoO}_2\text{F}_4$.

Magnetic Structure Determination from 5 K NPD Data. NPD data collected (on the GEM diffractometer) at 5 K were similar to those observed at 50 K, with some additional low-intensity peaks observed at long d-spacing (see the Supporting Information). Most of these peaks could be indexed by the same size unit cell as the nuclear structure, although a shoulder to the 102 peak ($\sim 12,700 \mu\text{s}$, 4.52 \AA) was not indexed by this unit cell. Attempts to index this peak using larger or lower-symmetry unit cells were unsuccessful.

High-resolution NPD data were also collected at 5 K, and although the strong reflections were consistent with those observed in the GEM data, some additional reflections on either side of some strong reflections were also observed. Attempts were made to fit these satellite reflections, but the reflections were fairly broad and low intensity, and our

attempts were not successful (stable refinements were not achieved). It is likely that they indicate an incommensurate modulation of the crystal structure, but their relatively broad nature may indicate a shorter correlation length of this modulation compared with the long-range average (commensurate) structure. Evidence for an incommensurate modulation in the crystal structure of another sample of $\text{Bi}_2\text{CoO}_2\text{F}_4$ has also been observed in electron diffraction data,⁵¹ but the possibility of vacancies on the anion sublattice, and slight differences in the O:F ratio, means that this incommensurate modulation could be quite sample-dependent. Our subsequent analysis is based on the average commensurate structure as determined from our NPD data collected on the GEM diffractometer.

ISODISTORT was used to explore possible magnetic structures to fit the 5 K (GEM) NPD data, assuming a $P2_1ab$ nuclear structure. Mode inclusion analysis (see the Supporting Information) suggested that models with an antiferromagnetic arrangement of moments in-plane gave good fits to the data. Two almost collinear models, $m\Gamma_1$ and $m\Gamma_2$ (see Figure 4a,b), give comparable fits to the data, and it

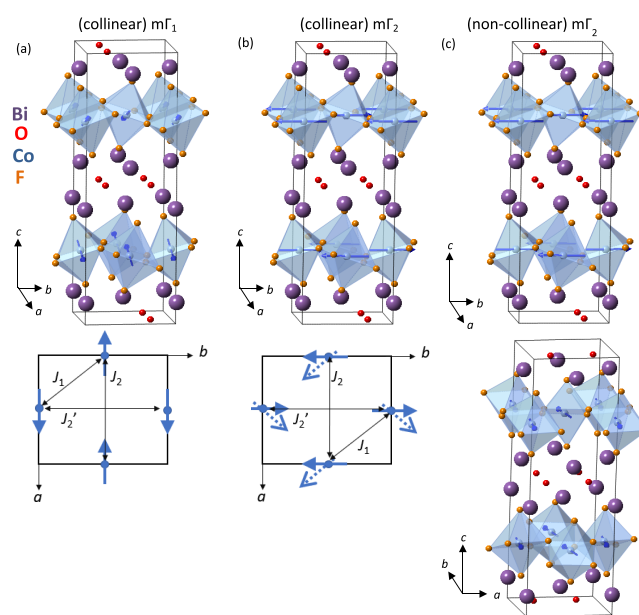


Figure 4. Schematic illustration of the $P2_1ab$ nuclear structure comparing (a) the collinear $m\Gamma_1$ magnetic structure and (b) the collinear $m\Gamma_2$ magnetic structure and (c) the final experimental $P2_1ab$ nuclear structure and the noncollinear $m\Gamma_2$ magnetic structure from refinements using 5 K NPD data. CoF_6 polyhedra are shown in pale blue, and Co^{2+} moments are shown by blue arrows; Co, Bi, F, and O sites are shown by blue, purple, orange, and red spheres, respectively. The bottom panels illustrate the approximately collinear arrangement of Co^{2+} moments (blue arrows) with the ab plane (with the noncollinear $m\Gamma_2$ model with FM component shown by dashed arrows), with the orthorhombic distortion exaggerated. nn J_1 and nnn J_2 and J_2' interactions are also illustrated.

is difficult to differentiate between these models from NPD data. The $m\Gamma_1$ model has Co^{2+} moments along the polar a axis, which is the axis about which CoF_6 octahedra rotate, similar to the intermediate-temperature magnetic model reported for La_2CoO_4 (with nuclear symmetry $Bmab$).⁵² The $m\Gamma_2$ model is similar but with Co^{2+} moments predominantly along the in-plane axis perpendicular to this (see Figure 4a,b). Given the

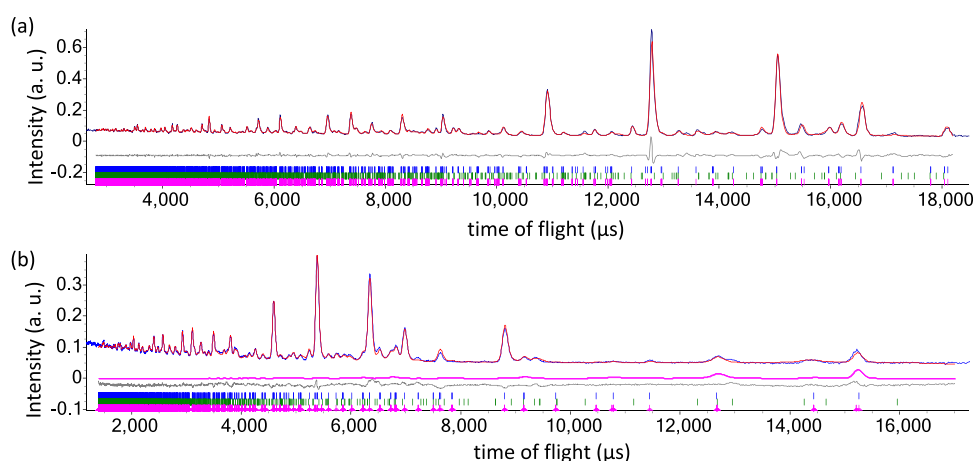


Figure 5. Details from Rietveld refinement using 5 K NPD data collected for $\text{Bi}_2\text{CoO}_2\text{F}_4$ using the $P2_1ab$ model (with anion vacancies) and $m\Gamma_2$ magnetic model. The refinement was carried out using NPD data from the 91° (panel a) and 35° (panel b) banks with upper ticks (blue) and middle ticks (green) showing peak positions for $\text{Bi}_2\text{CoO}_2\text{F}_4$ (86% by mass) and for $\text{Bi}_7\text{F}_{11}\text{O}_5$ (14% by mass), respectively; bottom ticks (pink) show positions of magnetic peaks, and the magnetic scattering is highlighted in pink. $R_{\text{wp}} = 5.83\%$, $R_p = 3.94\%$, and $\chi^2 = 14.2\%$.

tiny orthorhombic distortion observed, it is not surprising that these models give similar fits to our NPD data, and it is likely that these models are of similar energies. Interestingly, the $m\Gamma_2$ model allows an FM in-plane component (perhaps consistent with the low-field magnetic behavior evidenced by magnetization vs field measurements reported by Mitoudi Vagourdi et al.).²⁵ Further diffraction studies on single crystals (e.g., susceptibility measurements on single crystals or polarized neutron diffraction experiments) might allow these two models to be distinguished. Allowing this FM in-plane component to refine for the $m\Gamma_2$ model gave a stable refinement (although only small improvement in fit; R_{wp} decreased from 5.826 to 5.825% for this additional parameter), and a small nonzero FM component along $[100]$ was obtained ($0.7(2) \mu_{\text{B}}$), alongside the AFM component along $[010]$ ($2.37(7) \mu_{\text{B}}$), giving a total moment per Co^{2+} site of $2.5(1) \mu_{\text{B}}$ (further refinement details are given in the Supporting Information). Refinement details are given in Table 2 and profiles in Figure 5, with the final nuclear and magnetic structure illustrated in Figure 4c.

Density Functional Theory Calculations. Initial phonon calculations on the parent $I4/mmm$ model were used to determine key structural instabilities (to identify structural models for further spin-polarized calculations). Six unstable modes (which are all doubly degenerate) were identified: X_2^+ and X_3^+ rotations, Γ_5^- and M_5^+ polar and antipolar in-plane displacements (Figure 1), as well as another rotation mode X_4^+ ($a^-a^-c^0/-a^-a^-c^0$) and X_3^- in-plane antipolar displacements (see the Supporting Information). It is striking that the “rigid-layer” modes Γ_5^- and M_5^+ , which describe in-plane displacements of $[\text{Bi}_2\text{O}_2]^{2+}$ layers relative to the perovskite-like blocks (along $[110]_c$), are harder than often observed in perovskite-related Aurivillius phases.

Spin-polarized calculations were therefore carried out for the aristotype $I4/mmm$ model and for lower-symmetry models that allow these distortions (and are common ground states for $n = 1$ Aurivillius phases):

$$Pbca (X_3^+ \oplus X_2^+ \oplus M_5^+)$$

$$B2cb (X_3^+ \oplus \Gamma_5^-)$$

$$P2_1ab (X_3^+ \oplus X_2^+ \oplus \Gamma_5^-)$$

Three arrangements of Co^{2+} magnetic moments (Figure 6) were considered for each of the three nuclear structures: FM

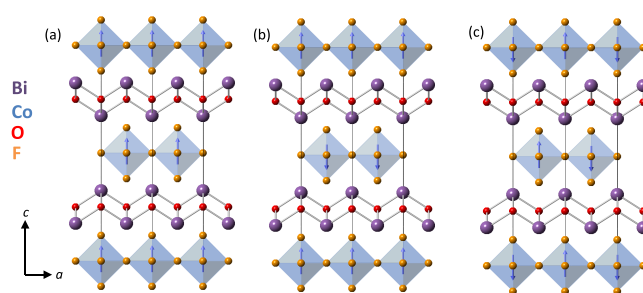


Figure 6. Schematic showing the three magnetic structures considered in spin-polarized DFT calculations: (a) FM, (b) AFM1 (with ferromagnetic intralayer interactions and antiferromagnetic interlayer interactions), and (c) AFM2 with intralayer and interlayer coupling both antiferromagnetic. CoF_6 polyhedra are shown in pale blue, and Co^{2+} moments are shown by blue arrows; Co, Bi, F, and O sites are shown by blue, purple, orange, and red spheres, respectively. (Anions are shown as small spheres for clarity.)

with all moments ferromagnetically aligned; AFM1 with ferromagnetic alignment within CoF_4 layers and antiferromagnetic coupling between layers; and AFM2 with antiferromagnetic CoF_4 layers. Preliminary calculations using LDA-JTH were inconclusive, being very sensitive to geometry optimization and giving results inconsistent with the experiment (see the Supporting Information).

Calculations using GGA-JTH gave the FM ground state for the $I4/mmm$ nuclear structure, but AFM2 ground states (with AFM1 next lowest in energy) for all the orthorhombic nuclear structures (for $U = 4$ and 6 eV; $J = 0.2, 0.4,$ and 0.6 eV), consistent with experimental results. Having established AFM2 as the ground state magnetic structure, it is interesting to compare the three nuclear models with the aristotype $I4/mmm$ model (with AFM2 spin order) (Table 3).

These results from DFT calculations are largely consistent with the experimental results discussed above, in terms of both the nuclear and magnetic structures.

DISCUSSION

Analysis of NPD data collected at 50 K suggests that “ $\text{Bi}_2\text{CoO}_2\text{F}_4$ ” may be slightly nonstoichiometric with anion vacancies. If these vacancies involve only F^- ions, the refined

Table 3. Relative Energies ΔE (meV per Formula Unit) and Mode Contributions (Calculated by AMPLIMODES)^{53,54} to the AFM2 Ground State Models for $\text{Bi}_2\text{CoO}_2\text{F}_4$ Relative to the $I4/mmm$ (AFM2) Model, for $U = 4$ eV and $J = 0.6$ eV

nuclear structure	mode contributions (Å)	ΔE (meV/f.u.)
$I4/mmm$		0
$Pbca$	$1.86 X_3^+ \oplus 1.14 X_2^+ \oplus 0.41 M_3^+$	-480
$B2cb$	$1.37 X_3^+ \oplus 0.011 \Gamma_5^-$	-871
$P2_1ab$	$2.02 X_3^+ \oplus 1.2 X_2^+ \oplus 0.011 \Gamma_5^- \oplus 0.59 M_3^+$	-874

occupancies would suggest a composition closer to $\text{Bi}_2\text{CoO}_2\text{F}_{3.32}$. This is reminiscent of reports on La_2CoO_3 ,⁸⁶ (prepared by the floating zone method under controlled atmosphere),⁵⁵ suggesting that cobalt ions may adopt an oxidation state <2 . This contrasts with a recent report on “ $\text{Bi}_2\text{MO}_2\text{F}_4$ ” ($M = \text{Fe}$ and Ni) analogues in which the stability of the $+2$ oxidation state for nickel gives stoichiometric $\text{Bi}_2\text{NiO}_2\text{F}_4$, while the iron analogue is Bi-deficient with $\text{Fe}^{+2/+3}$ cations.²⁷ Given that the XANES data suggest a cobalt oxidation state close to $+2$ (Figure 2), the possibility of some excess oxygen and a small degree of $\text{O}-\text{F}$ anti-site disorder ($\text{O}^{2-} \leftrightarrow 2\text{F}^-$, giving compositions $\text{Bi}_2\text{CoO}_{2+x/2}\text{F}_{4-x}$) seems likely (i.e., for the sample described in Table 1, the site occupancies would suggest $x \approx 1.38$, $\text{Bi}_2\text{CoO}_{2.69}\text{F}_{2.62}$). This would result in partial occupancy of some nominally “F” sites by vacancies and O^{2-} ions, consistent with site occupancies from NPD analysis (Table 1). The anion vacancies are largely concentrated on the equatorial sites, consistent with $\text{LaSrCoO}_{3.5-x}$ in which equatorial oxide vacancies occur to maintain the expected Co^{2+} oxidation state.⁴⁸ This illustrates the difficulty in preparing pure, stoichiometric Aurivillius oxyfluorides containing $d^n\text{B}$ -site cations. It is possible that the precise composition varies from sample to sample (and between batches) and may depend on the synthetic route.

The 50 K (above T_N) crystal structure of $\text{Bi}_2\text{CoO}_2\text{F}_4$ is orthorhombic, but it is striking that the unit cell is metrically very close to tetragonal ($a = 5.4343(5)$ Å, $b = 5.4339(6)$ Å), as reported for other $n = 1$ Aurivillius oxyfluorides (including $\text{Bi}_2\text{NbO}_5\text{F}$, $\text{Bi}_{1.8}\text{FeO}_2\text{F}_4$, and $\text{Bi}_2\text{NiO}_2\text{F}_4$).^{22,23,27} The orthorhombic crystal structure of $\text{Bi}_2\text{CoO}_2\text{F}_4$ of $P2_1ab$ symmetry can be described in terms of rotations of CoF_6 octahedra about the a axis (X_3^+ irrep; $a^-a^-c^0$ in Glazer notation relative to the parent structure of $I4/mmm$ symmetry) and about the long axis (X_2^+ irrep; a^0a^0c in Glazer notation), as well as small polar displacements of cations relative to anions along the polar a axis, as mapped out in the Supporting Information.¹⁷ Our analysis of diffraction data and the observed SHG activity indicate that $\text{Bi}_2\text{CoO}_2\text{F}_4$ adopts a crystal structure allowing both polar Γ_5^- displacements as well as rotation of CoF_6 about an in-plane axis (X_3^+ rotations).

Results from DFT calculations (Table 3 and the Supporting Information) are consistent with the experimental models described above, with lower-symmetry models calculated for all magnetic models dominated by X_3^+ ($a^-a^-c^0$) rotations of CoF_6 octahedra, with some further stabilization (and smaller contributions) from polar displacements (Γ_5^-) and X_2^+ ($a^0a^0c^n$) rotations.

If the only long-range ordered distortions are X_3^+ rotations and polar Γ_5^- displacements, then the model of $B2cb$ symmetry would seem most appropriate to describe the average long-range structure. It is difficult to confirm the $P2_1ab$ structure

(with long-range order of X_2^+ rotations) over a disordered model of $B2cb$ symmetry from our powder diffraction data, and a larger sample of higher purity would be needed for high-resolution NPD data or complementary electron diffraction studies. DFT results (Supporting Information) indicate that the X_2^+ mode is significantly softer than the polar Γ_5^- instability, and so the $P2_1ab$ ($X_3^+ \oplus X_2^+ \oplus \Gamma_5^-$) model seems the best description of the ground state. The difficulty in distinguishing between the disordered $B2cb$ and ordered $P2_1ab$ models experimentally is perhaps explained by their similar energies calculated by DFT (Table 3 and Supporting Information). It is possible that the second rotation mode, X_2^+ , condenses in on cooling, consistent with the disorder-order transition on cooling noted from Raman spectroscopy.²⁵

The Ruddlesden–Popper phase La_2CoO_4 (and related analogues) adopts a closely related structure of Bmb symmetry (for $135 \text{ K} < T < 408 \text{ K}$) with rotation of CoO_6 octahedra about the in-plane axis (X_3^+ rotations) but without further rotations or polar displacements.^{52,56,57} On further cooling, La_2CoO_4 undergoes a structural phase transition to tetragonal $P4_2/nm$ symmetry, in which the CoO_6 rotation axis (in-plane) rotates by 90° in successive layers.^{52,58} Models of $P4_2/nm$ symmetry were also considered for $\text{Bi}_2\text{CoO}_2\text{F}_4$ but gave fairly poor fits to the data (there was no clear change in peak widths from data at 50 K and at 5 K that might indicate a similar orthorhombic–tetragonal distortion for $\text{Bi}_2\text{CoO}_2\text{F}_4$). La_2CoO_4 contrasts with the Aurivillius oxide Bi_2WO_6 that adopts a polar ground state of $P2_1ab$ symmetry (allowing X_3^+ and X_2^+ rotations as well as Γ_5^- polar displacements).

The comparison between polar Bi_2WO_6 and $\text{Bi}_2\text{CoO}_2\text{F}_4$ with nonpolar Ruddlesden–Popper La_2CoO_4 perhaps highlights the role of the fluorite-like $[\text{Bi}_2\text{O}_2]^{2+}$ layers in the $n = 1$ Aurivillius phases that contain $6s^2 \text{Bi}^{3+}$ cations, known to favor lower-symmetry coordination environments.⁵⁹ However, while the Bi^{3+} cations may help stabilize these further distortions (X_2^+ tilts and polar displacements), the dominant contribution to the polarization is from the perovskite-like layers (apical F^- displacements and, to a lesser extent, Co^{2+} and equatorial F^- displacements), consistent with theory work on analogous Bi_2WO_6 .²⁰ Polar displacements of d^0 cations are often ascribed to the pseudo-Jahn–Teller effect,^{60–62} and this electronic driving force is lessened for d^n cations such as Co^{2+} here. Morita et al. explored the change in polarization with F-content in the series $\text{Bi}_2(\text{W,B})(\text{O,F})_6$ ($B = \text{Ta}$, Nb , and Ti) and noted that the polarization decreased noticeably with increasing F^- content.²⁴ This is likely explained by reduced cation–anion hybridization for more ionic fluoride-based systems,⁶³ increasing the importance of geometric drivers for distortions over electronic (pseudo-Jahn–Teller effect) factors.⁶⁴ This is consistent with polar Γ_5^- distortions being the softest instability for Bi_2WO_6 (and making similar contributions as X_3^+ and X_2^+ rotations to the ground state),⁶⁵ while the X_3^+ rotations are dominant for $\text{Bi}_2\text{CoO}_2\text{F}_4$ and Γ_5^- distortions make a much diminished contribution (Table 3 and Supporting Information). The reduced polarization as oxide ions are replaced by fluoride might also be a factor in the smaller orthorhombic distortion of the oxide-fluorides.^{22,23,27}

When analyzing the 5 K NPD data, we have tentatively described possible magnetic structures, assuming the $P2_1ab$ nuclear structure (on the assumption that the second tilt mode condenses in on cooling), but similar magnetic models can be derived for the $B2cb$ nuclear structure (see the Supporting

Information). Our analysis of the 5 K NPD data suggests that Co^{2+} moments are close to collinear (in zero applied magnetic field) with antiferromagnetic nearest-neighbor interactions, consistent with the negative Weiss temperature ($\theta = -142(2)$ K) determined by Mitoudi Vagourdi et al. (for $T > 150$ K in 7 T applied field).²⁵ The magnetic peaks are slightly broadened (particularly those with large l index) compared with the nuclear Bragg peaks, and this was fitted using a model to describe antiphase boundaries^{47,66} in the magnetic structure perpendicular to the c axis, with a magnetic correlation length $\xi_c \approx 60(10)$ Å at 5 K. This suggests that the in-plane magnetic exchange interactions are noticeably stronger than the interlayer exchange interactions. This is unsurprising given the layered crystal structure and is consistent with the 2D-like character reported for La_2CoO_4 .^{52,67} The size of the ordered Co^{2+} moment ($\sim 2.5 \mu_B$) is comparable to that reported for La_2CoO_4 ($2.9 \mu_B$)⁵² and close to the spin-only value often observed for high-spin Co^{2+} d^7 ions (in elongated D_{4h} coordination environments).⁶⁸ The magnetic models determined here for $\text{Bi}_2\text{CoO}_2\text{F}_4$ are close to the collinear AFM models described for the $Bmab$ phases of La_2CoO_4 and La_2NiO_4 ,⁵² with moments (close to) pointing toward an equatorial edge of the CoF_6 octahedra. Similar magnetic structures are reported for LaSrFeO_4 ^{69,70} and La_2NiO_4 ⁵² with $\text{Fe}^{3+}/\text{Ni}^{2+}$ spins in-plane and pointing toward an equatorial edge of the BO_6 octahedra. We note that the intermediate ($Bmab$) phase reported for (stoichiometric) La_2NiO_4 has Ni^{2+} moments directed along the axis of the tilts of NiO_6 octahedra,^{52,71} similar to the $m\Gamma_1$ model described here for $\text{Bi}_2\text{CoO}_2\text{F}_4$. The temperature below which 3D magnetic order emerges in $\text{Bi}_2\text{CoO}_2\text{F}_4$ (~ 75 K) is significantly lower than that for La_2CoO_4 (275 K), presumably reflecting the weakened interlayer interactions in $\text{Bi}_2\text{CoO}_2\text{F}_4$ due to the larger separation of Co^{2+} layers by fluorite-like $[\text{Bi}_2\text{O}_7]^{2+}$ layers (~ 8.1 Å at 5 K in $\text{Bi}_2\text{CoO}_2\text{F}_4$; ~ 6.1 Å at 10 K in La_2CoO_4).⁷²

Our magnetic structure refinements for $\text{Bi}_2\text{CoO}_2\text{F}_4$ (see above and the **Supporting Information**) suggest that Co^{2+} moments are close to in-plane, consistent with the largely XY-like anisotropy reported for La_2CoO_4 .⁶⁷ Inelastic neutron scattering work has found that the magnetism in La_2CoO_4 is dominated by AFM nearest-neighbor (nn) interactions (J_1 in **Figure 4**), while next-nearest-neighbor (nnn) interactions (J_2, J_2') are much weaker. This is consistent with the $m\Gamma_1$ and $m\Gamma_2$ models for $\text{Bi}_2\text{CoO}_2\text{F}_4$ that both allow AFM nn interactions (with the result that nnn pathways are FM and therefore frustrated).

There is a small Ising anisotropy reported for La_2CoO_4 that stabilizes the collinear magnetic model observed for the $Bmab$ phase ($135 < T < 275$ K), but this in-plane anisotropy is sufficiently small that on further cooling, the Co^{2+} moments rotate by 90° in successive layers (accompanied by an orthorhombic–tetragonal phase transition). Similar magnetocrystalline anisotropy might be expected for $\text{Bi}_2\text{CoO}_2\text{F}_4$, but the small orthorhombic distortion is likely to give little energy difference between the $m\Gamma_1$ and $m\Gamma_2$ models (with moments predominantly along $[100]$ and $[010]$ directions, respectively, of the $P2_1ab$ nuclear unit cell). Canting of the moments away from the collinear models may result from crystal field anisotropy of the Co^{2+} ions or from Dzyaloshinskii–Moriya (DM) exchange interactions, which would not be possible for the parent nuclear structure of $I4/mmm$ symmetry (with inversion centers along the nn Co–F–Co superexchange pathways).^{73,74} The magnetic field dependence observed in

susceptibility measurements for $\text{Bi}_2\text{CoO}_2\text{F}_4$ ²⁵ suggests that an applied magnetic field could also change the balance between these terms in the Hamiltonian. Measurements carried out in low magnetic fields show significant field dependence, consistent with a small ferromagnetic component (as might arise from canting of the moments, similar to that reported for Sr_2IrO_4 ⁷⁵), consistent with the $m\Gamma_2$ model. As the applied magnetic field increases, this FM component is reduced and $\text{Bi}_2\text{CoO}_2\text{F}_4$ behaves more like a collinear AFM (consistent with the $m\Gamma_1$ model).²⁵ It seems that an increased applied magnetic field stabilizes the collinear AFM $m\Gamma_1$ model for $\text{Bi}_2\text{CoO}_2\text{F}_4$ rather than the (canted) ferrimagnetic $m\Gamma_2$ model observed at low fields. Theory work to explore the relative energies of the exchange interactions and sources of anisotropy in $\text{Bi}_2\text{CoO}_2\text{F}_4$, as well as characterization using single crystals, would give further insights into this.

CONCLUSIONS

Our combined experimental and computational studies on $\text{Bi}_2\text{CoO}_2\text{F}_4$ have given insight into its structural and magnetic properties. The ground state structure is best described by polar $P2_1ab$ symmetry, analogous to the Aurivillius oxide ferroelectric Bi_2WO_6 .^{13,19} The magnetic ground state of $\text{Bi}_2\text{CoO}_2\text{F}_4$ is ferrimagnetic, arising from a small canting of otherwise collinear AFM arrangement of moments. This combination of polarity and FM component highlights the potential of Aurivillius oxide-fluorides for multiferroics and magnetoelectrics, particularly given the magnetostrictive effects observed at T_N in capacitance data for $\text{Bi}_2\text{FeO}_2\text{F}_4$.²⁷ However, our work has also identified some challenges: while replacing O^{2-} by F^- ions allows more magnetic ions to be accommodated by the perovskite-like layers (and gives similar magnetic behavior to the Ruddlesden–Popper oxides such as La_2CoO_4),^{52,67} the increased ionic character of the fluorides compared with oxides tends to reduce the stability of polar distortions, reducing the polarization.²⁴ It would be interesting to study the effect of concentrating F^- ions in the equatorial sites in the perovskite-like layers, leaving the apical sites fully occupied by O^{2-} .⁷⁶ This may give similar energies for the polar distortions involving $[\text{Bi}_2\text{O}_7]^{2+}$ layers to those observed in Bi_2WO_6 (although the polarization contribution from the perovskite-like layers is likely to remain diminished). Future work to explore the optimum O:F ratio and ordering for designing multiferroic and magnetoelectric Aurivillius oxide-fluorides would be valuable.

ASSOCIATED CONTENT

Supporting Information

The Supporting Information is available free of charge at <https://pubs.acs.org/doi/10.1021/acs.chemmater.2c02745>.

Analysis of variable temperature XRPD data, symmetry analysis for $n = 1$ Aurivillius phases, additional refinements (Rietveld and Pawley) using different models for 50 K and 5 K NPD data, selected bond lengths (and bond valence sum analysis) and angles from Rietveld refinements using NPD data, details of the magnetic structure investigation, and details from DFT calculations (PDF)

AUTHOR INFORMATION

Corresponding Author

Emma E. McCabe – School of Physical Sciences, University of Kent, Kent, Canterbury CT2 7NH, U.K.; Department of Physics, Durham University, Durham DH1 3LE, U.K.; orcid.org/0000-0001-5868-4570; Email: emma.mccabe@durham.ac.uk

Authors

Euan A. S. Scott – School of Physical Sciences, University of Kent, Kent, Canterbury CT2 7NH, U.K.

Eleni Mitoudi Vagourdi – Department of Materials and Environmental Chemistry, Stockholm University, SE-106 91 Stockholm, Sweden

Mats Johnsson – Department of Materials and Environmental Chemistry, Stockholm University, SE-106 91 Stockholm, Sweden; orcid.org/0000-0003-4319-1540

Vanessa Cascos – School of Physical Sciences, University of Kent, Canterbury CT2 7NH, U.K.

Filbin John – School of Physical Sciences, University of Kent, Canterbury CT2 7NH, U.K.

Dave Pickup – School of Physical Sciences, University of Kent, Canterbury CT2 7NH, U.K.

Alan V. Chadwick – School of Physical Sciences, University of Kent, Canterbury CT2 7NH, U.K.; orcid.org/0000-0002-6485-9207

Hania Djani – Centre de Développement des Technologies Avancées, Alger 16081, Algeria

Eric Bousquet – Theoretical Materials Physics, Q-MAT, CESAM, Université de Liège, Liège 4000, Belgium; orcid.org/0000-0002-9290-3463

Weiguo Zhang – Department of Chemistry, University of Houston, Houston, Texas 77204, United States

P. Shiv Halasyamani – Department of Chemistry, University of Houston, Houston, Texas 77204, United States; orcid.org/0000-0003-1787-1040

Complete contact information is available at: <https://pubs.acs.org/10.1021/acs.chemmater.2c02745>

Notes

The authors declare no competing financial interest.

ACKNOWLEDGMENTS

We thank funding agencies including the Royal Society (international exchange scheme IES\R3\170112), The Leverhulme Trust (RPG-2017-362), and EU COST Action “Towards oxide-based electronics”. F.J. is grateful to the Analytical Division of the Royal Society of Chemistry for a funding to support his summer internship. We are grateful to the ISIS Neutron and Muon Source (STFC) for the provision of beamtime and to Dr. Ivan da Silva for assistance with data collection. NPD data are available at <https://data.isis.stfc.ac.uk/doi/STUDY/105605763/>. We are grateful to Prof. T. Lancaster for helpful discussions. P.S.H. and W.Z. thank the Welch Foundation (grant E-1457) and the NSF (DMR-2002319) for support. XANES data were collected via the “ENERGY Materials” Block Allocation Grant at Diamond Light Source. E.M.V. and M.J. are grateful to the Swedish Research Council (VR) grant 2014-3931. Computational resources were provided by the Consortium des Equipements de Calcul Intensif (CECI) and the Tier-1 supercomputer of the Fédération Wallonie-Bruxelles.

REFERENCES

- (1) Hill, N. A. Why are there so few magnetic ferroelectrics? *J. Phys. Chem. B* **2000**, *104*, 6694–6709.
- (2) Spaldin, N. A.; Ramesh, R. Advances in magnetoelectric multiferroics. *Nat. Mater.* **2019**, *18*, 203–212.
- (3) Fang, P. H.; Robbins, C. R.; Aurivillius, B. Ferroelectricity In Compound $\text{Bi}_4\text{Ti}_3\text{O}_{12}$. *Phys. Rev.* **1962**, *126*, 892.
- (4) Dearaujo, C. A. P.; Cuchiaro, J. D.; McMillan, L. D.; Scott, M. C.; Scott, J. F. FATIGUE-FREE FERROELECTRIC CAPACITORS WITH PLATINUM-ELECTRODES. *Nature* **1995**, *374*, 627–629.
- (5) McCabe, E. E.; Greaves, C. Structural and magnetic characterisation of $\text{Bi}_2\text{Sr}_{1.4}\text{La}_{0.6}\text{Nb}_2\text{MnO}_{12}$ and its relationship to $\text{Bi}_2\text{Sr}_2\text{Nb}_2\text{MnO}_{12}$. *J. Mater. Chem.* **2005**, *15*, 177–182.
- (6) McCabe, E. E.; Greaves, C. Structural and magnetic characterisation of Aurivillius material $\text{Bi}_2\text{Sr}_2\text{Nb}_2.5\text{Fe}_0.5\text{O}_{12}$. *J. Solid State Chem.* **2008**, *181*, 3051–3056.
- (7) Giddings, A. T.; Stennett, M. C.; Reid, D. P.; McCabe, E. E.; Greaves, C.; Hyatt, N. C. Synthesis, structure and characterisation of the $n=4$ Aurivillius phase $\text{Bi}_5\text{Ti}_3\text{CrO}_{15}$. *J. Solid State Chem.* **2011**, *184*, 252–263.
- (8) Keeney, L.; Colfer, L.; Schmidt, M. Probing Ferroelectric Behavior in Sub-10 nm Bismuth-Rich Aurivillius Films by Piezoresponse Force Microscopy. *Microsc. Microanal.* **2022**, *28*, 1396–1406.
- (9) Halpin, J. C.; Schmidt, M.; Maity, T.; Pemble, M. E.; Keeney, L. Compositional Tuning of the Aurivillius Phase Material $\text{Bi}_5\text{Ti}_3-2x\text{Fe}_{1+x}\text{Nb}_x\text{O}_{15}$ ($0 \leq x \leq 0.4$) Grown by Chemical Solution Deposition and its Influence on the Structural, Magnetic, and Optical Properties of the Material. *IEEE Trans. Ultrason. Ferroelectr. Freq. Control* **2021**, *68*, 303–313.
- (10) Snedden, A.; Hervoches, C. H.; Lightfoot, P. Ferroelectric phase transitions in $\text{SrBi}_2\text{Nb}_2\text{O}_9$ and $\text{Bi}_5\text{Ti}_3\text{FeO}_{15}$: A powder neutron diffraction study. *Phys. Rev. B* **2003**, *67*, No. 092102.
- (11) Guo, Y.-Y.; Gibbs, A. S.; Perez-Mato, J. M.; Lightfoot, P. Unexpected phase transition sequence in the ferroelectric $\text{Bi}_4\text{Ti}_3\text{O}_{12}$. *IUCr* **2019**, *6*, 438–446.
- (12) Armstrong, R. A.; Newnham, R. E. Bismuth titanate solid solutions. *Mater. Res. Bull.* **1972**, *7*, 1025–1034.
- (13) McDowell, N. A.; Knight, K. S.; Lightfoot, P. Unusual high-temperature structural behaviour in ferroelectric Bi_2WO_6 . *Chemistry - a European Journal* **2006**, *12*, 1493–1499.
- (14) Knight, K. S. THE CRYSTAL STRUCTURE OF FERROELECTRIC Bi_2WO_6 AT 961 K. *Ferroelectrics* **1993**, *150*, 319–330.
- (15) Hatch, D. M.; Stokes, H. T.; Aleksandrov, K. S.; Misyul, S. V. Phase transitions in the perovskitelike A_2BX_4 structure. *Phys. Rev. B* **1989**, *39*, 9282–9288.
- (16) Hatch, D. M.; Stokes, H. T. Classification of octahedral tilting phases in the perovskite-like A_2BX_4 structure. *Phys. Rev. B* **1987**, *35*, 8509–8516.
- (17) Stokes, H. T.; Hatch, D. M.; Campbell, B. J.; Tanner, D. E. ISODISPLACE: a web-based tool for exploring structural distortions. *J. Appl. Crystallogr.* **2006**, *39*, 607–614.
- (18) Glazer, A. The classification of tilted octahedra in perovskites. *Acta Crystallogr., Sect. B: Struct. Sci.* **1972**, *28*, 3384–3392.
- (19) Knight, K. S. THE CRYSTAL-STRUCTURE OF RUSSELLITE - A REDETERMINATION USING NEUTRON POWDER DIFFRACTION OF SYNTHETIC Bi_2WO_6 . *Mineral. Mag.* **1992**, *56*, 399–409.
- (20) Djani, H.; Bousquet, E.; Kellou, A.; Ghosez, P. First-principles study of the ferroelectric Aurivillius phase Bi_2WO_6 . *Phys. Rev. B* **2012**, *86*, No. 054107.
- (21) Aurivillius, B. The structure of Bi_2NbOSF and isomorphous compounds. *Ark. Kemi* **1952**, *4*, 39–47.
- (22) Needs, R. L.; Dann, S. E.; Weller, M. T.; Cherryman, J. C.; Harris, R. K. The structure and oxide/fluoride ordering of the ferroelectrics $\text{Bi}_2\text{TiO}_4\text{F}_2$ and Bi_2NbOSF . *J. Mater. Chem.* **2005**, *15*, 2399–2407.

- (23) McCabe, E. E.; Jones, I. P.; Zhang, D.; Hyatt, N. C.; Greaves, C. Crystal structure and electrical characterisation of Bi₂NbOSF: an Aurivillius oxide fluoride. *J. Mater. Chem.* **2007**, *17*, 1193–1200.
- (24) Morita, K.; Park, J.-S.; Kim, S.; Yasuoka, K.; Walsh, A. Crystal Engineering of Bi₂WO₆ to Polar Aurivillius-Phase Oxyhalides. *J. Phys. Chem. C* **2019**, *123*, 29155–29161.
- (25) Mitoudi Vagourdi, E.; Müllner, S.; Lemmens, P.; Kremer, R. K.; Johnsson, M. Synthesis and Characterization of the Aurivillius Phase CoBi₂O₂F₄. *Inorg. Chem.* **2018**, *57*, 9115–9121.
- (26) Yu, X. W.; Mitoudi-Vagourdi, E.; Johnsson, M. The Aurivillius Compound CoBi₂O₂F₄ - an Efficient Catalyst for Electrolytic Water Oxidation after Liquid Exfoliation. *ChemCatChem* **2019**, *11*, 6105–6110.
- (27) Mentré, O.; Juárez-Rosete, M. A.; Colmont, M.; Ritter, C.; Fauth, F.; Duttine, M.; Huvé, M.; Terryn, C.; Duffort, V.; Arévalo-López, A. M. All-Magnetic Slabs and Multiferroism in (Bi_{2-x}O₂)-(MF₄) Aurivillius Oxyfluorides (M = Fe and Ni). *Chem. Mater.* **2022**, *34*, 5706–5716.
- (28) Coelho, A. A. *Topas Academic: General profile and structure analysis software for powder diffraction data*, Bruker AXS: Karlsruhe, Germany, 2012.
- (29) Coelho, A. TOPAS and TOPAS-Academic: an optimization program integrating computer algebra and crystallographic objects written in C++. *J. Appl. Crystallogr.* **2018**, *51*, 210–218.
- (30) Campbell, B. J.; Stokes, H. T.; Tanner, D. E.; Hatch, D. M. ISODISTORT. *J. Appl. Crystallogr.* **2006**, *39*, 607–614.
- (31) Petricek, V.; Dusek, M.; Palatinus, L. Crystallographic computing system Jana2006: general features. *Z. Kristallogr.* **2014**, *229*, 345–352.
- (32) Ok, K. M.; Chi, E. O.; Halasyamani, P. S. Bulk characterisation methods for non-centrosymmetric materials: second harmonic generation, piezoelectricity, pyroelectricity and ferroelectricity. *Chem. Soc. Rev.* **2006**, *35*, 710–717.
- (33) Hohenberg, P.; Kohn, W. INHOMOGENEOUS ELECTRON GAS. *Phys. Rev. B* **1964**, *136*, B864.
- (34) Gonze, X.; Amadon, B.; Anglade, P. M.; Beuken, J. M.; Bottin, F.; Boulanger, P.; Bruneval, F.; Caliste, D.; Caracas, R.; Cote, M.; Deutsch, T.; Genovese, L.; Ghosez, P.; Giantomassi, M.; Goedecker, S.; Hamann, D. R.; Hermet, P.; Jollet, F.; Jomard, G.; Leroux, S.; Mancini, M.; Mazevet, S.; Oliveira, M. J. T.; Onida, G.; Pouillon, Y.; Rangel, T.; Rignanese, G. M.; Sangalli, D.; Shaltaf, R.; Torrent, M.; Verstraete, M. J.; Zerah, G.; Zwanziger, J. W. ABINIT: First-principles approach to material and nanosystem properties. *Comput. Phys. Commun.* **2009**, *180*, 2582–2615.
- (35) Gonze, X.; Rignanese, G. M.; Verstraete, M.; Beuken, J. M.; Pouillon, Y.; Caracas, R.; Jollet, F.; Torrent, M.; Zerah, G.; Mikami, M.; Ghosez, P.; Veithen, M.; Ryt, J. Y.; Olevano, V.; Bruneval, F.; Reining, L.; Godby, R.; Onida, G.; Hamann, D. R.; Allan, D. C. A brief introduction to the ABINIT software package. *Zeitschrift Fur Kristallographie* **2005**, *220*, 558–562.
- (36) Blöchl, P. E. Projector augmented-wave method. *Phys. Rev. B* **1994**, *50*, 17953–17979.
- (37) Perdew, J. P.; Burke, K.; Ernzerhof, M. Generalized Gradient Approximation Made Simple. *Phys. Rev. Lett.* **1996**, *77*, 3865–3868.
- (38) Jollet, F.; Torrent, M.; Holzwarth, N. Generation of Projector Augmented-Wave atomic data: A 71 element validated table in the XML format. *Comput. Phys. Commun.* **2014**, *185*, 1246–1254.
- (39) Anisimov, V. I.; Gunnarsson, O. Density-functional calculation of effective Coulomb interactions in metals. *Phys. Rev. B* **1991**, *43*, 7570–7574.
- (40) Liechtenstein, A. I.; Anisimov, V. I.; Zaanen, J. Density-functional theory and strong interactions: Orbital ordering in Mott-Hubbard insulators. *Phys. Rev. B* **1995**, *52*, R5467–R5470.
- (41) Baroni, S.; de Gironcoli, S.; Dal Corso, A.; Giannozzi, P. Phonons and related crystal properties from density-functional perturbation theory. *Rev. Mod. Phys.* **2001**, *73*, 515–562.
- (42) Gonze, X.; Lee, C. Dynamical matrices, born effective charges, dielectric permittivity tensors, and interatomic force constants from density-functional perturbation theory. *Phys. Rev. B* **1997**, *55*, 10355–10368.
- (43) Berry, F. J.; Moore, E.; Mortimer, M.; Ren, X.; Heap, R.; Slater, P.; Thomas, M. F. Synthesis and structural characterisation of a new oxide fluoride of composition Ba₂SnO_{2.5}F_{3.x}H₂O (x=0.5). *J. Solid State Chem.* **2008**, *181*, 2185–2190.
- (44) Sears, V. F. *Neutron news* **1990**, *3*, 29–37.
- (45) McCabe, E. E.; Free, D. G.; Mendis, B. G.; Higgins, J. S.; Evans, J. S. O. Preparation, Characterization, and Structural Phase Transitions in a New Family of Semiconducting Transition Metal Oxychalcogenides β-La₂O₂MSe₂ (M=Mn, Fe). *Chem. Mater.* **2010**, *22*, 6171–6182.
- (46) Tuxworth, A. J.; McCabe, E. E.; Free, D. G.; Clark, S. J.; Evans, J. S. O. Structural Characterization and Physical Properties of the New Transition Metal Oxyselenide La₂O₂ZnSe₂. *Inorg. Chem.* **2013**, *52*, 2078–2085.
- (47) McCabe, E. E.; Stock, C.; Rodrigues, E. E.; Wills, A. S.; Taylor, J. W.; Evans, J. S. O. Weak spin interactions in Mott insulating La₂O₂Fe₂OSe₂. *Phys. Rev. B* **2014**, *89*, 100402.
- (48) Hayward, M. A.; Rosseinsky, M. J. Anion Vacancy Distribution and Magnetism in the New Reduced Layered Co(II)/Co(I) Phase LaSrCoO_{3.5-x}. *Chem. Mater.* **2000**, *12*, 2182–2195.
- (49) Brown, I. D.; Altermatt, D. Bond-valence parameters obtained from a systematic analysis of the inorganic crystal structure database. *Acta Cryst.* **1985**, *B41*, 244–247.
- (50) Brese, N. E.; O'Keefe, M. Bond-valence sum parameters for solids. *Acta Cryst.* **1991**, *B47*, 192–197.
- (51) Huvé, M.; Mentre, O.; Arevalo-Lopez, A., Incommensurate structural modulation in Bi₂CoO₂F₄. private communication, 2022.
- (52) Yamada, K.; Matsuda, M.; Endoh, Y.; Keimer, B.; Birgeneau, R. J.; Onodera, S.; Mizusaki, J.; Matsuura, T.; Shirane, G. Successive antiferromagnetic phase transitions in single-crystal La₂CoO₄. *Phys. Rev. B* **1989**, *39*, 2336.
- (53) Perez-Mato, J. M.; Orobengoa, D.; Aroyo, M. I. Mode crystallography of distorted structures. *Acta Crystallogr., Sect. A: Found. Adv.* **2010**, *66*, 558–590.
- (54) Orobengoa, D.; Capillas, C.; Aroyo, M. I.; Perez-Mato, J. M. AMPLIMODES: symmetry-mode analysis on the Bilbao Crystallographic Server. *J. Appl. Crystallogr.* **2009**, *42*, 820–833.
- (55) Furukawa, Y.; Wada, S.; Kajitani, T.; Hosoya, S. 59Co Zero-Field NMR Study of Antiferromagnetism in Low-Temperature Tetragonal Phase of La₂CoO_{3.86}. *J. Phys. Soc. Jpn.* **1999**, *68*, 346–349.
- (56) Birgeneau, R. J.; Chen, C. Y.; Gabbe, D. R.; Janssen, H. P.; Kastner, M. A.; Peters, C. J.; Picone, P. J.; Thio, T.; Thurston, T. R.; Tuller, H. L.; Axe, J. D.; Böni, P.; Shirane, G. Soft-phonon behavior and transport in single-crystal La₂CuO₄. *Phys. Rev. Lett.* **1987**, *59*, 1329–1332.
- (57) Böni, P.; Axe, J. D.; Shirane, G.; Birgeneau, R. J.; Gabbe, D. R.; Janssen, H. P.; Kastner, M. A.; Peters, C. J.; Picone, P. J.; Thurston, T. R. Lattice instability and soft phonons in single-crystal La_{2-x}Sr_xCuO₄. *Phys. Rev. B* **1988**, *38*, 185–194.
- (58) Heger, G.; Mullen, D.; Knorr, K. On the importance of hydrogen bonding for the structural phase transitions in (CH₃NH₃)-2MnCl₄. A single-crystal neutron diffraction study. *Phys. Status Solidi A* **1976**, *35*, 627–637.
- (59) Walsh, A.; Payne, D. J.; Egdell, R. G.; Watson, G. W. Stereochemistry of post-transition metal oxides: revision of the classical lone pair model. *Chem. Soc. Rev.* **2011**, *40*, 4455–4463.
- (60) Ok, K. M.; Halasyamani, P. S.; Casanova, D.; Llunell, M.; Alemany, P.; Alvarez, S. Distortions in Octahedrally Coordinated d0 Transition Metal Oxides: A Continuous Symmetry Measures Approach. *Chem. Mater.* **2006**, *18*, 3176–3183.
- (61) Eng, H. W.; Barnes, P. W.; Auer, B. M.; Woodward, P. M. Investigations of the electronic structure of d0 transition metal oxides belonging to the perovskite family. *J. Solid State Chem.* **2003**, *175*, 94–109.
- (62) Kang, S. K.; Albright, T. A.; Eisenstein, O. THE STRUCTURE OF D0 ML₆ COMPLEXES. *Inorg. Chem.* **1989**, *28*, 1611–1613.

(63) Woodward, P. M.; Karen, P.; Evans, J. S. O.; Vogt, T., *Solid state materials chemistry*. Cambridge University Press: 2021, DOI: 10.1017/9781139025348.

(64) Garcia-Castro, A. C.; Spaldin, N. A.; Romero, A. H.; Bousquet, E. Geometric ferroelectricity in fluoroperovskites. *Phys. Rev. B* **2014**, *89*, No. 104107.

(65) Djani, H.; Hermet, P.; Ghosez, P. First-Principles Characterization of the P21ab Ferroelectric Phase of Aurivillius Bi_2WO_6 . *J. Phys. Chem. C* **2014**, *118*, 13514–13524.

(66) Her, J.-H.; Stephens, P. W.; Gao, Y.; Soloveichik, G. L.; Rijssenbeek, J.; Andrus, M.; Zhao, J.-C. Structure of unsolvated magnesium borohydride $\text{Mg}(\text{BH}_4)_2$. *Acta Cryst* **2007**, *63*, 561–568.

(67) Babkevich, P.; Prabhakaran, D.; Frost, C. D.; Boothroyd, A. T. Magnetic spectrum of the two-dimensional antiferromagnet La_2CoO_4 studied by inelastic neutron scattering. *Phys. Rev. B* **2010**, *82*, No. 184425.

(68) Matsumoto, Y.; Nambu, Y.; Honda, T.; Ikeda, K.; Otomo, T.; Kageyama, H. High-pressure Synthesis of $\text{Ba}_2\text{CoO}_2\text{Ag}_2\text{Te}_2$ with Extended CoO_2 Planes. *Inorg. Chem.* **2020**, *59*, 8121–8126.

(69) Qureshi, N.; Ulbrich, H.; Sidis, Y.; Cousson, A.; Braden, M. Magnetic structure and magnon dispersion in LaSrFeO_4 . *Phys. Rev. B* **2013**, *87*, No. 054433.

(70) Jung, M. H.; Alsmadi, A. M.; Chang, S.; Fitzsimmons, M. R.; Zhao, Y.; Lacerda, A. H.; Kawanaka, H.; El-Khatib, S.; Nakotte, H. Magnetic ordering in single-crystalline SrLaFeO_4 and $\text{Sr}_{1.1}\text{La}_{0.9}\text{FeO}_4$. *J. Appl. Phys.* **2005**, *97*, 10A926.

(71) Rodriguez-Carvajal, J.; Fernandez-Diaz, M. T.; Martinez, J. L. Neutron diffraction study on structural and magnetic properties of La_2NiO_4 . *J. Phys.: Condens. Matter* **1991**, *3*, 3215–3234.

(72) Le Dréau, L.; Prestipino, C.; Hernandez, O.; Schefer, J.; Vaughan, G.; Paofai, S.; Perez-Mato, J. M.; Hosoya, S.; Paulus, W. Structural Modulation and Phase Transitions in $\text{La}_2\text{CoO}_{4.14}$ Investigated by Synchrotron X-ray and Neutron Single-Crystal Diffraction. *Inorg. Chem.* **2012**, *51*, 9789–9798.

(73) Yosida, K., *Theory of Magnetism*. 1 ed.; Springer Berlin: Heidelberg, 1996.

(74) Moskvina, A. Dzyaloshinskii–Moriya Coupling in 3d Insulators. *Condensed Matter* **2019**, *4*, 84.

(75) Crawford, M. K.; Subramanian, M. A.; Harlow, R. L.; Fernandez-Baca, J. A.; Wang, Z. R.; Johnston, D. C. Structural and magnetic studies of Sr_2IrO_4 . *Phys. Rev. B* **1994**, *49*, 9198–9201.

(76) Wang, J.; Shin, Y.; Paudel, J. R.; Grassi, J. D.; Sah, R. K.; Yang, W.; Karapetrova, E.; Zaidan, A.; Strocov, V. N.; Klewe, C.; Shafer, P.; Gray, A. X.; Rondinelli, J. M.; May, S. J. Strain-Induced Anion-Site Occupancy in Perovskite Oxyfluoride Films. *Chem. Mater.* **2021**, *33*, 1811–1820.

Recommended by ACS

MIO_3F (M = Co and Ni): Magnetic Iodate Fluorides with Zigzag Chains

Hang Liu, Hongcheng Lu, *et al.*

OCTOBER 26, 2022
INORGANIC CHEMISTRY

READ 

Lead-Free Aurivillius Phase $\text{Bi}_2\text{LaNb}_{1.5}\text{Mn}_{0.5}\text{O}_9$: Structure, Ferroelectric, Magnetic, and Magnetodielectric Effects

Tio Putra Wendari, Zulhadjri Zulhadjri, *et al.*

MAY 27, 2022
INORGANIC CHEMISTRY

READ 

Influence of Barium Intercalated Ions on Magnetic Interaction in the Tellurate Compound $\text{BaNi}_2\text{TeO}_6$

Yujie Song, Zhengcai Xia, *et al.*

APRIL 06, 2022
INORGANIC CHEMISTRY

READ 

Synthesis and Characterization of Magnetolectric $\text{Ba}_7\text{Mn}_4\text{O}_{15}$

Gabriel R. M. Clarke, Mark S. Senn, *et al.*

JUNE 21, 2022
INORGANIC CHEMISTRY

READ 

Get More Suggestions >